Check for updates

Efficient free-space to on-chip coupling of THz-bandwidth pulses for biomolecule fingerprint sensing

YANBING QIU,[1] KUN MENG,[2] WANLIN WANG,[1] JING CHEN,[1] JOHN CUNNINGHAM,[3] IAN ROBERTSON,[3] BINBIN HONG,[1,3,4] AND GUO PING WANG[1,5]

[1]*College of Electronics and Information Engineering, Shenzhen University, Shenzhen 518060, China*
[2]*Qingdao QUENDA Terahertz Technology Co. Ltd, Qingdao 266104, China*
[3]*School of Electronic and Electrical Engineering, University of Leeds, Leeds LS2 9JT, UK*
[4]*b.hong@szu.edu.cn*
[5]*gpwang@szu.edu.cn*

Abstract: Wide bandwidth THz pulses can be used to record the distinctive spectral fingerprints related to the vibrational or rotational modes of polycrystalline biomolecules, and can be used to resolve the time-dependent dynamics of such systems. Waveguides, owing to their tight spatial confinement of the electromagnetic fields and the longer interaction distance, are promising platforms with which to study small volumes of such systems. The efficient input of sub-ps THz pulses into waveguides is challenging owing to the wide bandwidth of the THz signal. Here, we propose a sensing chip comprised of a pair of back-to-back Vivaldi antennas feeding into, and out from, a 90° bent slotline waveguide to overcome this problem. The effective operating bandwidth of the sensing chip ranges from 0.2 to 1.15 THz, and the free-space to on-chip coupling efficiency is as high as 51% at 0.44 THz. Over the entire band, the THz signal is ~42 dB above the noise level at room temperature, with a peak of ~73 dB above the noise. In order to demonstrate the use of the chip, we have measured the characteristic fingerprint of α-lactose monohydrate, and its sharp absorption peak at ~0.53 THz was successfully observed, demonstrating the promise of our technique. The chip has the merits of efficient in-plane coupling, ultra-wide bandwidth, ease-of-integration, and simple fabrication. It has the potential for large-scale manufacture, and can be a strong candidate for integration into other THz light-matter interaction platforms.

1. Introduction

Sub-ps THz pulses conveying ultra-wideband spectral information can be used to resolve the time-dependent ultrafast dynamics of molecules which are associated with vibrational and rotational motions, and long-range intermolecular interactions [1,2]. The light-matter interaction between the ultra-wideband sub-ps THz pulses and the materials to be tested have recently been active research areas, seeking to reveal the physical mechanisms associated with the intrinsic properties of the materials, including spectral fingerprints, dielectric properties, carrier lifetimes, etc. [3] THz light paths are often inefficient when interacting with nanomaterials owing to their ultra-small quantity and volume being a poor match to the larger size of diffraction-limited free-space focused THz waves. Waveguides have thus been widely developed to be able to enhance the light-matter interaction through the tight spatial confinement of electromagnetic fields and the longer interaction distance they provide.

Recently, THz waveguides, which can confine electromagnetic fields into deep-subwavelength regions and hence further break the diffraction limit, have been shown to be very promising

platforms for this, with the potential for enhancing light-matter coupling [4]. However, there are several challenges to realizing strong interaction between the sub-ps THz pulse and the nanomaterials on/in waveguides. To efficiently utilize the large bandwidth of sub-ps THz pulses, the waveguides conveying the signal have, firstly, to be able to support single-mode operation over decades of bandwidth. Many THz waveguides or fibers are tailored for low-loss wave propagation by using modes that do not support such wide operating bandwidth. These include photonic crystal fibers [5–11], microstructure fibers [12–15], step-index fibers [16–18], substrate-integrated waveguides [19], and silicon waveguides [20–22]. In contrast, some classic metallic waveguides support ultra-wideband single-mode operation that can guide the THz pulse, including parallel-plate waveguide [23,24], microstrip [25], coplanar waveguide [26], slotline [27], metal wires [28–30], and the Goubau line [31].

A further challenge is found in the method of coupling the ultra-wideband sub-ps THz pulse into the waveguide. One way is to excite and detect the THz pulse in-situ in the transmission line, for example with integrated LT-GaAs based photoconductive switches [26,31,32–45]. This technique has a high degree of integration (both the photoconductive emitter and detector are integrated on the chip), small footprint, and low signal distortion caused by the air humidity (the THz signal is tightly guided around the transmission lines instead of the free space), but it also requires a complex fabrication process as well as high fabrication and material costs. Another method is to couple the THz pulse into the waveguides using external THz sources. THz time-domain spectroscopy (THz-TDS) is commonly used in this scenario. D. Grischkowsky et al. experimentally reported a quasi-optical method to couple sub-ps THz pulse into submillimeter circular metal waveguides using hyper hemispherical silicon lenses in 1999 [46]. The following year, the same group used a cylindrical lens to couple the sub-ps THz pulse into plastic ribbon waveguides [47]. Owing to the large group-velocity dispersion of both circular metal waveguides and plastic ribbon waveguides, the received THz pulses are highly dispersive, however. In 2001, an ultra-wideband THz signal ranging from 0.1 to 4 THz was coupled into a parallel-plate waveguide using cylindrical dielectric lenses [23]. Since then, owing to the excellent performances in bandwidth, loss, and dispersion, parallel-plate waveguides have widely been studied [48,49], and many guided THz spectroscopy applications based on the parallel-plate waveguide have been demonstrated to detect the fingerprints of water, biological molecules, etc. [48,50]. However, despite their advantages, parallel-plate waveguides are relatively bulky and inflexible for bending and integration which limits their large-scale application. In 2004, D. M. Mittleman et al. experimentally demonstrated the free-space to bare metal wires coupling of a THz signal using focusing lenses and scattering input coupler, and the transmitted signal is dispersionless, with a bandwidth of about 0.1-0.5 THz [28]. In addition to time-domain methods, frequency-domain spectroscopy using electronic-based sources and detectors has also been studied. For example, M. Unlu et al. reported that an antenna array could be used to couple the continuous-wave THz wave into a spoof surface plasmon polariton waveguide [51]. J. Xie et al. demonstrated an out-of-plane THz free-space to silicon waveguide coupling technique using a grating and a compact spotsize converter, operating from 170 to 220 GHz with a coupling loss of about 5 dB at 194 GHz [52]. Usually, however, electronic-based frequency-domain spectroscopy (FDS) is relatively narrowband and has thus rarely been used for fingerprint detection.

Here, we numerically investigate and experimentally demonstrate an efficient in-plane free-space to on-chip coupling of ultra-wideband sub-ps THz pulses using ultra-wideband Vivaldi antennas. The sensing chip is comprised of a pair of back-to-back Vivaldi antennas and a 90° bent slotline waveguide. The sensing chip can easily be fabricated using photolithography and metal physical vapor deposition on a large scale with high consistency and low cost. Owing to the flat form of the sensing chip and the in-plane coupling, the chip is highly compatible with commercial THz-TDS and FDS instruments. In addition, we also demonstrate the detection of the biomolecule vibration fingerprint by placing the α-lactose monohydrate powders on the

90° bent slotline waveguide region. The proposed THz sensing chip with an efficient in-plane coupling function can be a promising platform for ultra-wideband light-matter interaction.

2.   Design and performances of the sensing chip

The sensing chip consists of a Vivaldi antenna at each end, and a section of slotline waveguide with a 90° bend. Vivaldi antennas are chosen due to their flat form, in-plane coupling, broad bandwidth, low cross-polarization, easy integration, and ease of fabrication [53]. A schematic diagram of the sensing chip, manufactured on polyimide (PI), is shown in Fig. 1(a). The slotline waveguide supports quasi-TEM mode over a broad band with tight electromagnetic field confinement [27]. Polyimide, with its excellent heat resistance, fine strength, rigidity, and compatibility with microfabrication processes, is one of the best organic polymer materials available, with a good combination of properties. A 13-μm-thick film is chosen as this suppresses competition from high-order substrate modes, allowing only the fundamental slotline mode to propagate. The two back-to-back Vivaldi antennas have the same specifications and dimensions. The length and the opening width of the Vivaldi antenna were 1.6 mm (ℓ) and 0.62 mm (w), respectively. Here, the top curvature of the right Vivaldi antenna followed an exponential function, a $y = A(e^{Bx} - 1) + \frac{s}{2}$, where A and B are geometrical coefficients, and s is the width of the waveguide. The origin of coordinate is placed at the center of the joint interface between the 90° bent slotline waveguide and the right Vivaldi antenna.
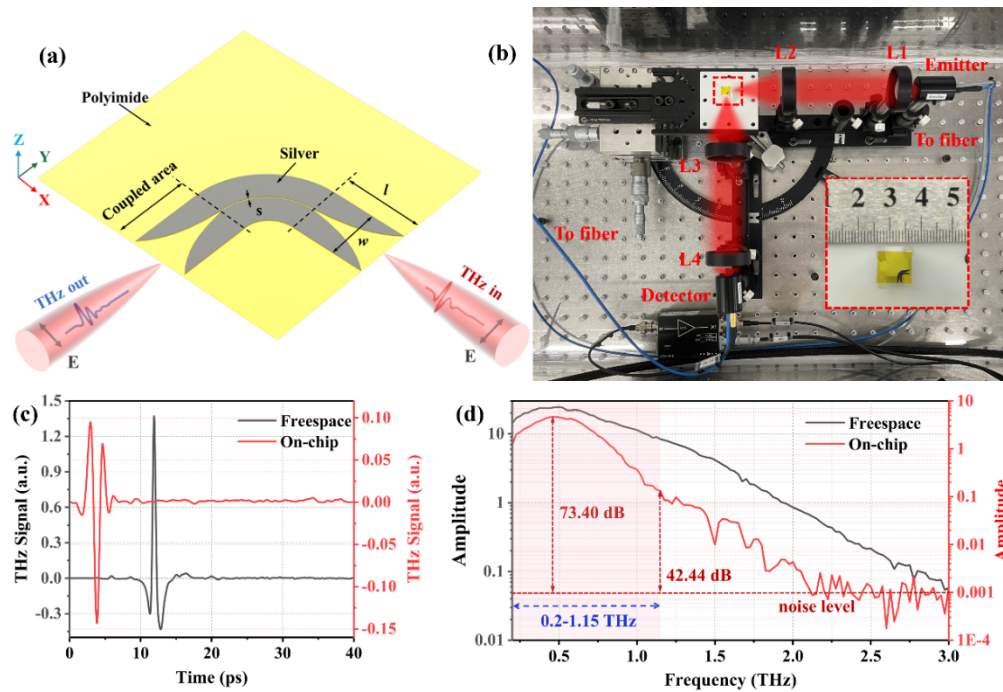

Fig. 1. Schematic, experimental set-up, and measurement results of the free-space to on-chip coupling system. (a) Sensing chip schematic diagram. (b) Experimental set-up. L1, L2, L3, and L4 are TPX lenses. Emitter and Detector refer to the THz photoconductive antennas. The red semi-transparent region indicates the optical path of the THz signal. The inset diagram shows the fabricated sensing chip. (c) Free-space (black) and on-chip (red) time domain signals obtained using terahertz time-domain spectroscopy (THz-TDS) system; (d) Free-space (black) and on-chip (red) spectra.

The sensing chip was fabricated using a lift-off technique. The 13-µm-thick DuPont Kapton PI film firstly was adhered to a 450-µm-thick silicon wafer to keep the PI film flat during the fabrication process. The sacrificial adhesive layer between the PI film and the silicon wafer was a spin-coated 1.4 µm thick AR-N 4340 negative photoresist layer that would eventually be dissolved in acetone. Separate from the above adhesive layer, another AR-N 4340 photoresist layer was spin-coated onto the PI film at 4000 rpm for 60 s. After baking the coated structure at 90°C for 1 min to completely evaporate the solvent, a 1.4 µm thick resist film was obtained. The pattern of the sensing chip was transferred from a pre-prepared photomask to the resist film by photo exposure. For patterning the resist, the exposure dose of the UV light was 140 mJ/cm^2. The exposed resist film was baked at 95°C for 2 min for crosslinking. The post-baked film was developed in AR 300-47 developer at 21°C for 60 s and then was rinsed in DI-H$_2$O for 30 s. After that, a 10-nm-thick titanium layer, a 300-nm-thick silver layer, and a 10-nm-thick titanium layer were deposited sequentially on top of the partially covered PI substrate and the patterned photoresist layer by electron-beam evaporation. The first titanium layer acts as an adhesive layer between the PI film and the silver layer, while the second titanium layer is a protective layer preventing the rapid oxidation of the silver layer. Silver was chosen due to its high conductivity, to reduce the Ohmic loss. Then, both photoresist layers, including the patterned layer above the PI substrate and the sacrificial adhesive layer between the PI substrate and the silicon wafer, were dissolved in acetone and rinsed in DI-H$_2$O. Finally, the sensing chip was successfully patterned on the PI substrate using the lift-off technique, and was then separated from the silicon wafer after dissolving the sacrificial adhesive layer.

The width of the channel (*s*) in the curved slotline waveguide was set to be 25 µm, which is approximately one-twenty fourth of the representative wavelength at 500 GHz (the peak of the THz spectrum). The slotline waveguide was intentionally designed with a 90° bend so that the polarizations of the THz signals are orthogonal to each other at the input and the output ends. This eliminates the unwanted line-of-sight signals which are not coupled into the slotline waveguide, to make the received signal more distinct.

Figure 1(b) shows the experimental set-up used for testing the sensing chip, and the inset shows an optical image of the fabricated sensing chip. A commercial fiber-coupled THz-TDS system based on a 1560 nm femtosecond fiber laser (TERA K15, MenloSystems Corp.) was used to focus the THz radiation into the slotline waveguide with the help of terahertz TPX (Polymethyl Pentene) lenses. The fiber-coupled THz emitter and receiver use an InP-based InGaAs/InAlAs multilayer structure as the photoconductive materials for emitting and detecting the THz signals. As shown in the diagram, the emitted terahertz signal is coupled into the sensing chip by the Vivaldi antenna after diverging at the lens L1 and converging at the lens L2. Afterwards, the THz signal was transmitted through the curved slotline waveguide and then coupled into free space by the second Vivaldi antenna. Finally, it passed through the lenses L3 and L4 and was received by the detector. Here, the focal lengths of all TPX lenses are 50 mm. The sensing chip was attached to a 3D-printed holder, fixed to a three-axes adjustable stage to aid the alignment of the THz signal. The system was sealed in an acrylic box, with any effects from water absorption during measurements eliminated by purging with dry nitrogen. The THz-TDS signals shown in Fig. 1(c) were measured using this experimental system. The unloaded time-domain signal passing through the chip (red curve) was obtained using the chip with 90° bend, as shown in Fig. 1(b), while the free-space time-domain signal (black curve) was obtained from a testing system with a straight optical path without any chip. A time window of 40 ps was applied to the time-domain signals to avoid the Fabry-Perot effect, which results in a frequency resolution of about 7.35 GHz. Figure 1(d) shows the THz amplitude spectra after performing a fast Fourier transform (FFT) on the measured time-domain signals shown in Fig. 1(c). It can be seen that the effective operating frequency band of the sensing chip is 0.2-1.15 THz (indicated by the red shaded area). Over this operating band, the overall dynamic range of the terahertz signal is larger

than 42 dB, with the highest one reaching ~73 dB. As there are significant dips that occurred at around 1.23 THz and 1.5 THz, caused by unwanted resonances on the chip, so we consider the effective operating band is slightly below this frequency point to obtain a relatively clean transmission window. The reproducibility of the measurement has been experimentally verified by comparing the time-domain signals and frequency-domain spectra of different samples or different times of measurements using the same sample, and we have found that the variations are small and thus the measurements are reliable and reproducible.

3. Vivaldi antenna optimization for enhancing the coupling efficiency

The directivity of the Vivaldi antenna is one of the key factors that affects the overall coupling efficiency between the free-space terahertz beam and the guided slotline mode. The Vivaldi antenna acts differently at the input and output ends. At the input end, the antenna there receives a concentrated THz beam originally emitted from a photoconductive dipole antenna. The concentrated THz beam has a good transverse Gaussian shape, confirmed by measurement using an iris. At the output end, meanwhile, its radiation pattern is shown in Fig. 2. Figure 2 shows the far-field radiation patterns for five Vivaldi antennas with different lengths, at several representative frequency points. The geometrical coefficients *A* and *B* chosen correspond to five antenna lengths as shown in Table 1. These far-field diagrams were simulated using CST Microwave Studio. The Time-Domain Solver was used to calculate the propagation field patterns of the slotline waveguide and the Vivaldi antenna. The frequency-dependent permittivity of the PI, and the conductivity of the silver, are obtained from the CST material library. The typical permittivity of the PI at 1 THz is $\varepsilon = \varepsilon' + i\varepsilon''$, where $\varepsilon' = 3.4215$ and $\varepsilon'' = 0.0095$ [54]. The typical conductivity of the silver is 6.3012×10^7 S/m. The boundary conditions in all directions are set to be open. For simplicity, the surface roughness resulting from fabrication tolerances was not included in the simulation.
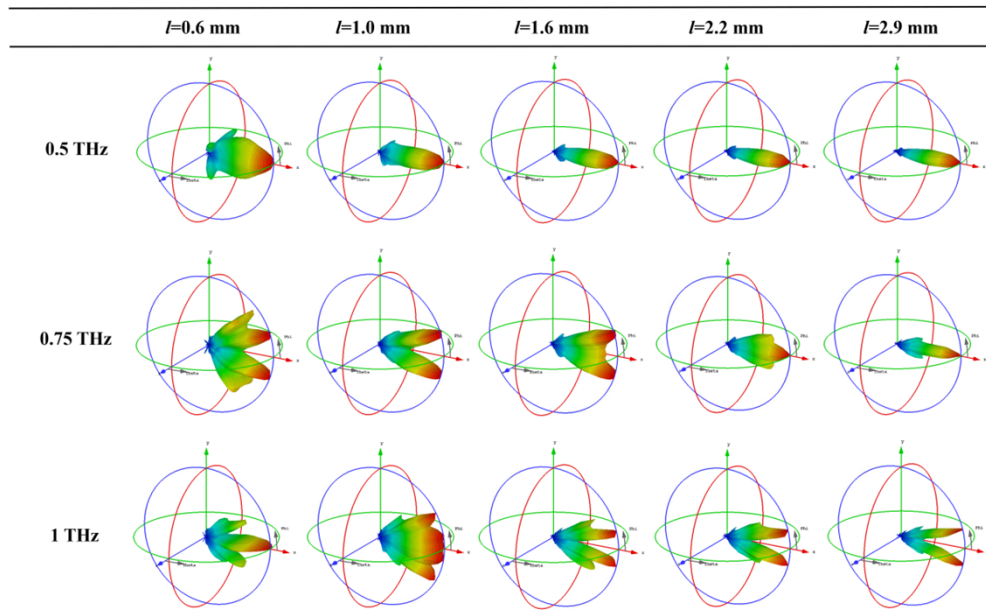

Fig. 2. Simulated far-field radiation patterns of the Vivaldi antennas with different lengths at several representative frequency points. The widths of the Vivaldi antennas (w) and the channel of the slotline waveguide are all fixed as 0.62 mm and 25 µm, respectively.

Table 1. The geometrical coefficients of the representative Vivaldi antennas with different lengths

	$l = 0.6\,\text{mm}$	$l = 1.0\,\text{mm}$	$l = 1.6\,\text{mm}$	$l = 2.2\,\text{mm}$	$l = 2.9\,\text{mm}$
A	0.535	0.0375	0.026	0.015	0.0145
B	4.2	2.85	2	1.7	1.3

Ideally, a Vivaldi antenna with high directivity over a wide band is preferred, but owing to the limit of the intrinsic bandwidth of the Vivaldi antenna, the radiation patterns of the Vivaldi antennas diverge significantly towards high frequencies, as shown in Fig. 2. Besides, it can be seen that the Vivaldi antenna with a longer antenna length has better directivity, but at the same time it will also introduce greater Ohmic loss. Thus, a balance between good directivity and low insertion loss has to be considered in the design. It should be noted that the focal length and the diameter of the L2 and L3 TPX lenses used to focus and collimate the THz signal are 50 mm and 38 mm, respectively, which indicates the maximum ray angle against the axis is $\theta_0 = 20.8°$. Therefore, the THz field radiated by the Vivaldi antenna at the output end with a radiation angle large than θ_0 will not be picked up by the L3 lens. On the other hand, the L3 lens can pick up the THz field up to the largest angle of 20.8°, suggesting that the coupling scheme can tolerate the divergence of the Vivaldi antenna at high THz frequencies.

Along with the directivity, the reflection coefficient (S_{11}) also specifies the degree of coupling provided by Vivaldi antenna, as shown in Fig. 3(a). Here, Vivaldi antennas with different lengths and a fixed width are fed by a slotline waveguide with a fixed gap width of 25 μm. Comparing Fig. 3(a) with Fig. 2, although the directivity of the Vivaldi antenna with $l = 2.9$ mm is best among the five selected representative lengths, its reflection coefficient is the largest. Generally, it can be seen from Fig. 3(a) that the Vivaldi antennas support wideband operation since their reflection coefficient is low between 0.2 and 2 THz. At the low THz frequency end, the reflection coefficients are relatively large, indicating that the impedance mismatch between the Vivaldi antenna using the proposed geometric properties and the long wavelength THz free-space wave is stronger. Apart from the case of $l = 2.9$ mm, the reflection coefficients of other Vivaldi antennas are basically below -10 dB between 0.5 and 2 THz. Among the five selected representative Vivaldi antennas, the longer Vivaldi antenna shows better directivity, while the shorter antenna shows a lower reflection coefficient, and the overall coupling coefficient is affected by both factors. THz sensing chips with these five representative Vivaldi antennas were fabricated, and their performance measured for comparison.

Figure 3(c) shows the experimentally measured total insertion losses of the chips (L_{total}) with different Vivaldi antennas. They are determined using the following equation:

$$L_{\text{total}} = -20 \times \log_{10}\left(\frac{A_{\text{chip}}}{A_{\text{fs}}}\right). \tag{1}$$

Here, A_{fs} denotes the frequency domain amplitude of the free-space THz signal measured using a straight THz optical path without the chip being placed between the L2 and the L3 lenses, as shown using a black solid line in Fig. 1(d). A_{chip} denotes the amplitude of the on-chip THz signal measured using the 90° bent THz path, with the chip being placed between the L2 and the L3 lenses, an example of which has been illustrated using a red solid line in Fig. 1(d). It can be seen from Fig. 3(c) that the overall performance of the chip with the $l = 1.6$ mm Vivaldi antenna is optimal, as it averagely has a minimum total loss across the frequency band of interest from 0.2 to 1.15 THz. In addition, the ripples, which are caused by impedance mismatch and unwanted resonances on the chip, are also minimal for $l = 1.6$ mm.

The insertion loss of a single Vivaldi antenna (L_{ant}) can be obtained using the following expression:

$$L_{\text{ant}} = \frac{L_{total} - L_{wg}}{2}, \tag{2}$$
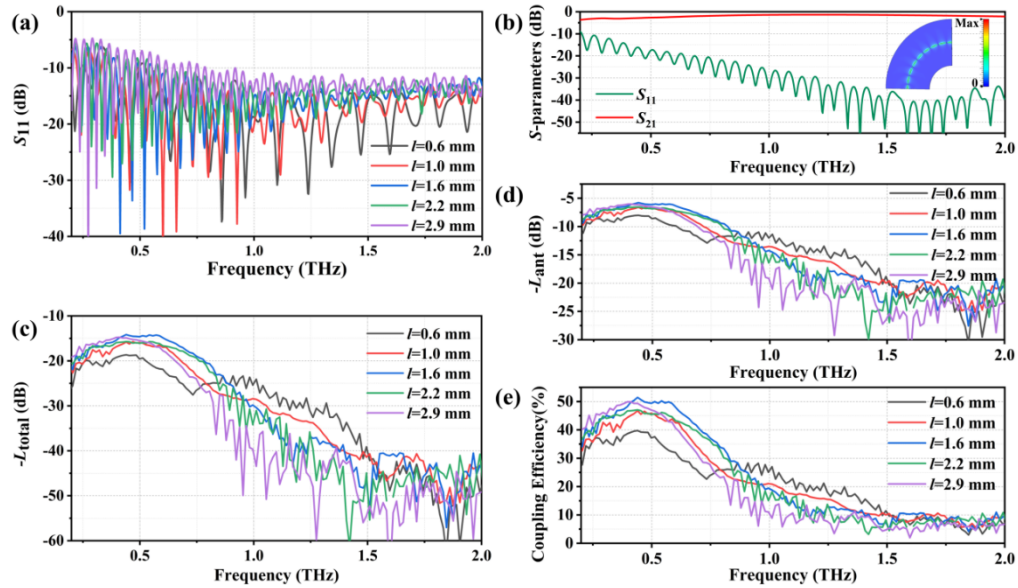
Fig. 3. Simulated and measured performances of the Vivaldi antennas and the slotline waveguide. (a) The simulated reflection coefficients of antennas with different lengths. (b) The simulated transmission coefficients and reflection coefficients of bent waveguide. (a) and (b) are numerically calculated using CST time-domain solver. (c) The measured total insertion losses of the sensing chips. (d) The measured insertion loss of a single Vivaldi antenna. (e) The measured coupling efficiency of a single Vivaldi antenna. (c)-(e) are measured using THz-TDS.

where L_{wg} is the insertion loss of the 90° bent slotline waveguide. It should be noted that L_{wg} must be obtained numerically based on CST simulation, owing to the lack of a robust way to extract its value experimentally. It is a reasonable approximation because the slotline waveguide with 25 µm gap width supports the wideband single-mode operation and the 90° bent structure is smooth and produces no undesired resonances. The dispersion of the dielectric properties of the polyimide substrate, and the conductivity of the silver layer, were taken into account in the simulation. The parameter L_{wg} is equivalent to the transmission coefficient (S_{21}) of the 90° bent slotline waveguide, as shown in Fig. 3(c). It can be seen that the slotline waveguide supports wideband transmission between 0.2 THz and 2 THz, and its insertion loss ranges from 1.36 dB to 3.66 dB. Furthermore, the inset presents the normalized electric field propagating along the bent waveguide at 0.5 THz, which shows that the THz field is tightly confined around the gap of the slotline waveguide. The insertion losses of the Vivaldi antennas calculated using Eq. (2) are shown in Fig. 3(d). The Vivaldi antenna with a length of 1.6 mm is still the best, with the minimum loss of only 5.77 dB occurring at 0.44 THz.

Finally, the coupling efficiency of a single Vivaldi antenna on the chip can be calculated as follows:

$$\eta = 10^{\frac{-L_{ant}}{20}} \times 100\%. \tag{3}$$

The calculated results are shown in Fig. 3(e). It can be seen that the overall coupling efficiency of the antenna with a length of 1.6 mm can reach 50%, which is the most optimal among different antennas. The decline of the coupling efficiency at low- and high-frequency ends is due to the large impedance mismatch caused by the significant size differences between the characteristic

geometrical size of the Vivaldi antennas and the wavelengths of the free-space electromagnetic waves.

Figure 4 shows the radiation patterns of Vivaldi antennas with different widths at the output end. Their corresponding tentative geometrical coefficients are given in Table 2. It can be seen that the radiation directivities of the antennas gradually weaken at high frequencies. This property is similar to that of the antennas with different lengths discussed in Fig. 2. Meanwhile, among the five selected antennas, the antennas with 0.45 mm and 0.62 mm opening widths show a better relative balance between high directivity and low return loss, which will be further explored in Fig. 5(a). In contrast, antennas with smaller and larger widths exhibit relatively poor radiative directivity at 0.5 THz. At the same time, the reflection coefficients of the antennas have also been simulated, and the results are shown in Fig. 5(a). Comparing Fig. 4 with Fig. 5(a), although the directivity of the Vivaldi antenna with $w = 0.28$ mm is the best among the five selected representative antennas, its reflection coefficient is also the largest. In addition, the reflectance coefficients of the antennas with widths of 0.62, 0.79, and 0.96 mm are very similar and are smaller than that of the antenna with $w = 0.45$ mm. Taking these observations into consideration, two chips with antenna widths of 0.45 and 0.62 mm were fabricated and measured. The reason for this choice was that the antenna with a width of 0.45 mm shows excellent radiative directivity, while the antenna with $w = 0.62$ mm shows a better reflection coefficient. It is difficult to further compare the potential performances of the chips with the antennas width of 0.45 and 0.62 mm merely using the simulation results, since both the directivity and the reflection coefficient affect the overall coupling efficiency and a tradeoff has to be made between them. Thus, we fabricated and measured the two chips to experimentally determine which one performs better.
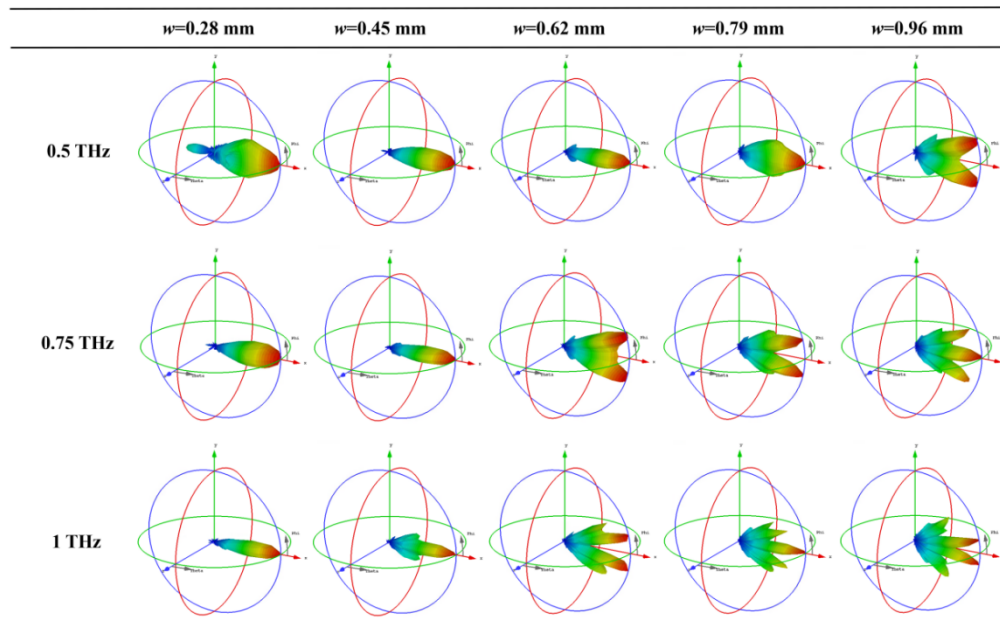

Fig. 4. Simulated far-field radiation patterns of the Vivaldi antennas with different widths at several representative frequency points. The length of the Vivaldi antennas (l) and the central channel width (s) of the slotline waveguide are fixed as 1.6 mm and 25 μm, respectively.

Figure 5(b) shows the experimentally measured $-L_{total}$ of the sensing chip with different Vivaldi antennas, calculated using Eq. (1). It can be seen that the case with $w = 0.62$ mm has a lower total loss than the other. Besides, the spectrum of the former case is relatively smoother
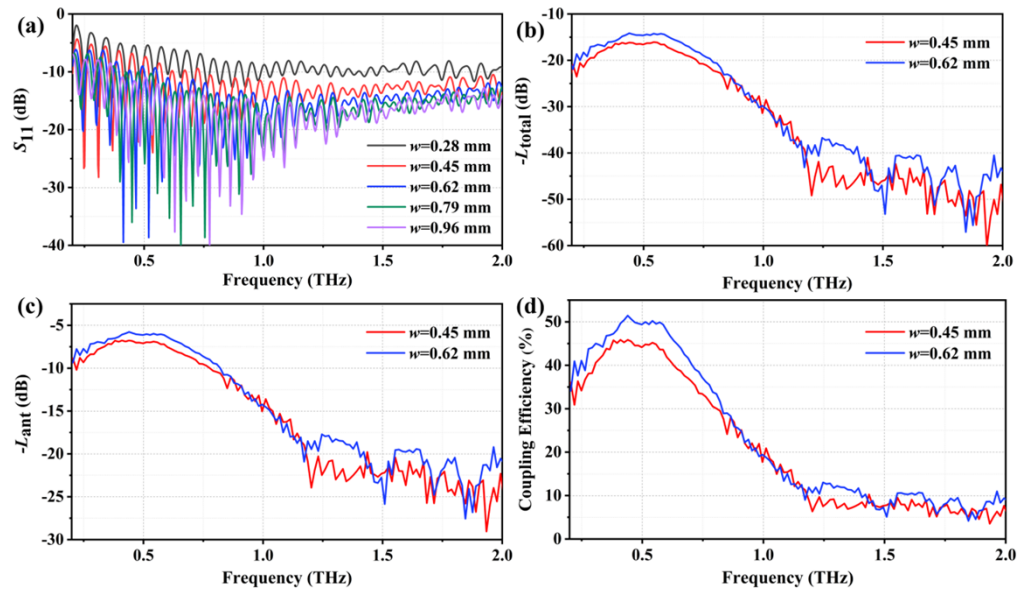
Fig. 5. Simulated and measured performances of the Vivaldi antennas with different widths. (a) The simulated reflection coefficients of antennas with different widths, which are numerically calculated using CST time-domain solver. (b) The measured total insertion losses of the sensing chips. (c) The measured insertion loss of a single Vivaldi antenna. (d) The measured coupling efficiency of a single Vivaldi antenna. (b)-(d) are measured using THz-TDS.

Table 2. The geometrical coefficients of the representative Vivaldi antennas with different widths

	$w = 0.28$ mm	$w = 0.45$ mm	$w = 0.62$ mm	$w = 0.79$ mm	$w = 0.96$ mm
A	0.026	0.026	0.026	0.026	0.026
B	1.52	1.8	2	2.15	2.265

than the latter one below 1 THz, which is more preferable for sensing applications. Figure 5(c) presents the insertion losses of the one-side Vivaldi antennas on the chips, obtained using Eq. (2). Here, same as Fig. 3(d), the insertion loss of the 90° bent slotline waveguide used to calculate the L_{ant} is given in Fig. 3(b). The Vivaldi antenna with $w = 0.62$ mm shows lower insertion loss over a wide frequency band. Finally, the calculated coupling efficiencies of the two Vivaldi antennas are shown in Fig. 5(d). It can be concluded from Figs. 5(b) to 5(d) that the Vivaldi antenna with $w = 0.62$ mm is superior to the other antenna with $w = 0.45$ mm in terms of the total loss, single antenna loss, spectrum smoothness, and coupling efficiency. Hence, the former design was chosen for the proof-of-concept THz fingerprint sensing, shown in Fig. 6.
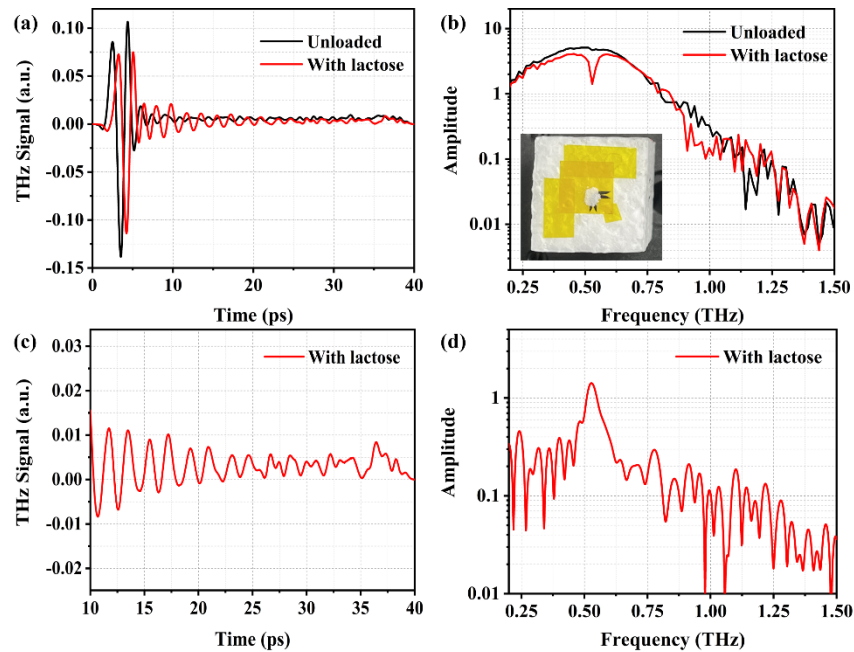
Fig. 6. The THz signals and spectra with and without the α-lactose monohydrate powders on the chip. (a)The measured time-domain signals with and without (unloaded) the α-lactose monohydrate powders; (b) Frequency spectra related to the signals shown in (a). The inset diagram shows the sensing chip with α-lactose monohydrate powder added. The mass of the monohydrate powder is 1.0 mg. The sensing chip is placed on the top of an EPS foam block; (c) Truncated signal with lactose, extracted from (a); (d) The frequency spectrum of (c).

4. On-chip biomolecule fingerprint sensing

To take advantage of the sensing chip with efficient free-space to on-chip coupling, we investigated use of the chip for spectroscopy. The THz regime has abundant distinctive spectral fingerprints relating to the vibration and rotation of biomolecules, offering many potential applications in biomedical sensing and imaging [55]. α-lactose monohydrate is a widely studied biomolecule that has a THz absorption fingerprint at around 0.53 THz when in polycrystalline form, owing to an external hindered rotational mode along the B-axis of the α-lactose crystal with intermolecular hydrogen-bond networks [56,57]. Therefore, the α-lactose monohydrate is an ideal candidate to demonstrate and evaluate the fingerprint sensing ability of the proposed sensing chip.

The interaction between the ultra-wideband THz pulse and the α-lactose monohydrate happens on the slotline waveguide region of the sensing chip, where the electromagnetic field is tightly confined at the deep-subwavelength scale, enhancing the interaction efficiency. Figure 6 shows the measured time-resolved signals and their spectra calculated using FFT (Fast Fourier Transform) of the above light-matter interaction processes. Figure 6(a) compares the time-domain signals of the THz waves passing through the sensing chip with (red curve, loaded chip) and without (black curve, unloaded chip) using 1.0 mg α-lactose monohydrate powders. The signal with lactose on the chip is delayed and attenuated compared with the unloaded one, and shows additional resonances after the main peak attributed to absorption.

Figure 6(b) presents the frequency spectra calculated based on Fig. 6(a) using the FFT. The inset shows a photo of the chip with monohydrate powder sample placed on a low-density expanded polystyrene (EPS) foam block. The mass of the monohydrate powder is 1.0 mg. The

EPS foam is dispersionless and low-loss [58]. According to our measurement using THz-TDS, over the frequency range of interest from 0.2 to 2 THz, its refractive index is very close to that of air at 1.006, with negligible variations, and its absorption is extremely low which is less than $0.35\,\text{cm}^{-1}$. Thus, the supporting EPS foam is expected to have a limited impact on the transmission properties of the proposed chip. The EPS foam has good mechanical stability thus supporting the polyimide-based chip firmly when adding the monohydrate samples. In the figure, a sharp absorption dip near 0.53 THz can be observed from the red curve, which does not appear on the black curve, indicating that the chip can efficiently sense the THz fingerprint of the monohydrate in a small quantity. At frequencies above 0.75 THz, the spectra of the unloaded and loaded chip both exhibit ripples due to the unwanted impedance mismatches occurring on the chip and also in the free-space optical system, which limits the useful bandwidth of the proposed chip. Comparing Fig. 6(b) with Fig. 1(d), the reduction of the effective bandwidth of the smooth spectrum is due to the introduction of the EPS foam block as the substrate. It may be possible to extend the bandwidth with further optimization of the design and the experimental set-up, and by making use of calibration techniques.

Figures 6(a) and 6(d) show the truncated time-domain signal between 10 to 40 ps, extracted from Fig. 6(a), and its corresponding spectrum. The main peak in the frequency spectrum occurs at near 0.53 THz, indicating the damped fluctuation in Fig. 6(a) is mainly caused by the hindered rotational mode of the α-lactose crystal. Consequently, we have successfully experimentally demonstrated a wideband and efficient method to excite the THz deep-subwavelength mode of the slotline waveguide via the Vivaldi antenna, which can be used as a platform for detecting the THz fingerprints of biomolecules on a chip. Further efforts can be made to broaden the smooth spectrum of the sensing chip in future works, including eliminating the resonance dips on the high-end of the spectrum by breaking the resonance condition and using another more rigid and flatter substrate rather than the PI film.

5. Conclusions

In summary, we have proposed a sensing chip that is comprised of a pair of back-to-back Vivaldi antennas and a 90° bent slotline waveguide, to overcome the challenge of efficient free-space to on-chip coupling, as well as benefitting from enhanced light-matter interaction on the chip. The coupling efficiency and fingerprint sensing ability of the proposed chip have been numerically investigated and experimentally demonstrated. With the help of Vivaldi antennas, the in-plane free-space to on-chip coupling efficiency is up to 50% in the operating frequency range from 0.2 to 1.15 THz. The amplitude of the THz signal is 42 dB above the noise level across the entire operating band, with a peak of 73 dB. On-chip fingerprint sensing of α-lactose monohydrate has been performed and an absorption dip at near 0.53 THz has been observed. The proposed sensing chip with efficient free-space to on-chip coupling can be a promising platform in which to study light-matter interaction using sub-ps THz pulses, with potential relevance to many materials and systems.

References

1. L. Ho, M. Pepper, and P. Taday, "Signatures and fingerprints," Nat. Photonics **2**(9), 541–543 (2008).
2. A. G. Davies, A. D. Burnett, W. Fan, E. H. Linfield, and J. E. Cunningham, "Terahertz spectroscopy of explosives and drugs," Mater. Today (Oxford, U. K.) **11**(3), 18–26 (2008).
3. D. Nicoletti and A. Cavalleri, "Nonlinear light–matter interaction at terahertz frequencies," Adv. Opt. Photon. **8**(3), 401–464 (2016).
4. X. Q. Zhang, Q. Xu, L. B. Xia, Y. F. Li, J. Q. Gu, Z. Tian, C. M. Ouyang, J. G. Han, and W. L. Zhang, "Terahertz surface plasmonic waves: a review," Adv. Photon. **2**(01), 1 (2020).
5. A. Dupuis, K. Stoeffler, B. Ung, C. Dubois, and M. Skorobogatiy, "Transmission measurements of hollow-core THz Bragg fibers," J. Opt. Soc. Am. B **28**(4), 896–907 (2011).
6. B. Hong, M. Swithenbank, N. Somjit, J. Cunningham, and I. Robertson, "Asymptotically single-mode small-core terahertz Bragg fibre with low loss and low dispersion," J. Phys. D: Appl. Phys. **50**(4), 045104 (2017).
7. B. Hong, M. Swithenbank, N. Greenall, R. G. Clarke, N. Chudpooti, P. Akkaraekthalin, N. Somjit, J. E. Cunningham, and I. D. Robertson, "Low-loss asymptotically singlemode THz Bragg fiber fabricated by digital light processing rapid prototyping," IEEE Trans. THz Sci. Technol. **8**(1), 90–99 (2018).
8. B. Hong, N. Chudpooti, P. Akkaraekthalin, N. Somjit, J. Cunningham, and I. Robertson, "Investigation of electromagnetic mode transition and filtering of an asymptotically single-mode hollow THz Bragg fibre," J. Phys. D: Appl. Phys. **51**(30), 305101 (2018).
9. J. Li, K. Nallappan, H. Guerboukha, and M. Skorobogatiy, "3D printed hollow core terahertz Bragg waveguides with defect layers for surface sensing applications," Opt. Express **25**(4), 4126 (2017).
10. Z. Wu, W. R. Ng, M. E. Gehm, and H. Xin, "Terahertz electromagnetic crystal waveguide fabricated by polymer jetting rapid prototyping," Opt. Express **19**(5), 3962 (2011).
11. J. Yang, J. Zhao, C. Gong, H. Tian, L. Sun, P. Chen, L. Lin, and W. Liu, "3D printed low-loss THz waveguide based on Kagome photonic crystal structure," Opt. Express **24**(20), 22454–60 (2016).
12. V. Setti, L. Vincetti, and A. Argyros, "Flexible tube lattice fibers for terahertz applications," Opt. Express **21**(3), 3388 (2013).
13. W. Lu, S. Lou, and A. Argyros, "Investigation of flexible lowloss hollow-core fibres with tube-lattice cladding for terahertz radiation," IEEE J. Select. Topics Quantum Electron. **22**(2), 214–220 (2016).
14. K. Nielsen, "Bendable, low-loss Topas fibers for the terahertzfrequency range," Opt. Express **17**(10), 8592–8601 (2009).
15. J. Anthony, R. Leonhardt, A. Argyros, and M. C. Large, "Characterization of a microstructured Zeonex terahertz fiber," J. Opt. Soc. Am. B **28**(5), 1013–1018 (2011).
16. K. Nallappan, Y. Cao, G. Xu, H. Guerboukha, C. Nerguizian, and M. Skorobogatiy, "Dispersion-limited versus power-limited terahertz communication links using solid core subwavelength dielectric fibers," Photonics Res. **8**(11), 1757–1775 (2020).
17. H. Guerboukha, G. Yan, O. Skorobogata, and M. Skorobogatiy, "Silk foam terahertz waveguides," Adv. Opt. Mater. **2**(12), 1181–1192 (2014).
18. B. Hong, Y. Qiu, N. Somjit, J. Cunningham, I. Robertson, and G. P. Wang, "Guidance of Terahertz Wave over Commercial Optical Fiber," In *Proceedings of IEEE Conference on 46th International Conference on Infrared, Millimeter and Terahertz Waves* (IEEE, 2021), pp, 1–2.
19. F. Fesharaki, T. Djerafi, M. Chaker, and K. Wu, "Guided-wave properties of mode-selective transmission line," IEEE Access **6**, 5379–5392 (2018).
20. K. Tsuruda, M. Fujita, and T. Nagatsuma, "Extremely low-loss teraertz waveguide based on silicon photonic-crystal slab," Opt. Express **23**(25), 31977–31990 (2015).
21. H. Amarloo and S. Safavi-Naeini, "Terahertz Line Defect Waveguide Based on Silicon-on-Glass Technology," IEEE Trans. THz Sci. Technol. **7**(4), 433–439 (2017).
22. W. Gao, X. Yu, M. Fujita, T. Nagatsuma, C. Fumeaux, and W. Withayachumnankul, "Effective-medium-cladded dielectric waveguides for terahertz waves," Opt. Express **27**(26), 38721–38734 (2019).
23. R. Mendis and D. Grischkowsky, "Undistorted guided-wave propagation of subpicosecond terahertz pulses," Opt. Lett. **26**(11), 846–848 (2001).
24. R. Mendis and D. Grischkowsky, "THz interconnect with low-loss and low-group velocity dispersion," IEEE Microw. Wireless Compon. Lett. **11**(11), 444–446 (2001).
25. H. M. Heiliger, M. Nagel, H. G. Roskos, H. Kurz, F. Schnieder, W. Heinrich, and K. Ploog, "Low-dispersion thin-film microstrip lines with cyclotene (benzocyclobutene) as dielectric medium," Appl. Phys. Lett. **70**(17), 2233–2235 (1997).
26. M. B. Ketchen, D. Grischkowsky, T. C. Chen, C. C. Chi, I. N. Duling Iii, N. J. Halas, and G. P. Li, "Generation of subpicosecond electrical pulses on coplanar transmission lines," Appl. Phys. Lett. **48**(12), 751–753 (1986).
27. H. Pahlevaninezhad, B. Heshmat, and T. E. Darcie, "Efficient terahertz slot-line waveguides," Opt. Express **19**(26), B47–B55 (2011).
28. K. Wang and D. M. Mittleman, "Metal wires for terahertz wave guiding," Nature **432**(7015), 376–379 (2004).
29. T. I. Jeon, J. Zhang, and D. J. Grischkowsky, "THz Sommerfeld wave propagation on a single metal wire," Appl. Phys. Lett. **86**(16), 161904 (2005).

30. A. Markov, H. Guerboukha, and M. Skorobogatiy, "Hybrid metal wire–dielectric terahertz waveguides: challenges and opportunities," J. Opt. Soc. Am. B **31**(11), 2587–2600 (2014).

31. C. Russell, C. D. Wood, A. D. Burnett, L. Li, E. H. Linfield, A. G. Davies, and J. E. Cunningham, "Spectroscopy of polycrystalline materials using thinned-substrate planar Goubau line at cryogenic temperatures," Lab Chip **13**(20), 4065–4070 (2013).

32. D. R. Grischkowsky, "Optoelectronic characterization of transmission lines and waveguides by terahertz time-domain spectroscopy," IEEE J. Select. Topics Quantum Electron. **6**(6), 1122–1135 (2000).

33. M. B. Byrne, J. Cunningham, K. Tych, A. D. Burnett, M. R. Stringer, C. D. Wood, L. Dazhang, M. Lachab, E. H. Linfield, and A. G. Davies, "Terahertz vibrational absorption spectroscopy using microstrip-line waveguides," Appl. Phys. Lett. **93**(18), 182904 (2008).

34. S. Yanagi, M. Onuma, J. Kitagawa, and Y. Kadoya, "Propagation of terahertz pulses on coplanar strip-lines on low permittivity substrates and a spectroscopy application," Appl. Phys. Express **1**(1), 012009 (2008).

35. S. Kasai, A. Tanabashi, K. Kajiki, T. Itsuji, R. Kurosaka, H. Yoneyama, M. Yamashita, H. Ito, and T. Ouchi, "Micro strip line-based on-chip terahertz integrated devices for high sensitivity biosensors," Appl. Phys. Express **2**(6), 062401 (2009).

36. J. Kitagawa, Y. Kadoya, K. Suekuni, M. A. Avila, and T. Takabatake, "Characterization of terahertz absorption in clathrate compound by compact spectroscopic chip," Jpn. J. Appl. Phys. **52**(2R), 028003 (2013).

37. J. B. Wu, O. Sydoruk, A. S. Mayorov, C. D. Wood, D. Mistry, L. H. Li, E. H. Linfield, A. G. Davies, and J. E. Cunningham, "Time-domain measurement of terahertz frequency magnetoplasmon resonances in a two-dimensional electron system by the direct injection of picosecond pulsed currents," Appl. Phys. Lett. **108**(9), 091109 (2016).

38. C. Russell, M. Swithenbank, C. D. Wood, A. D. Burnett, L. H. Li, E. H. Linfield, A. G. Davies, and J. E. Cunningham, "Integrated on-chip THz sensors for fluidic systems fabricated using flexible polyimide films," IEEE Trans. THz Sci. Technol. **6**(4), 619–624 (2016).

39. J. Zuo, L. L. Zhang, C. Gong, and C. L. Zhang, "Research progress of super-continuum terahertz source based on nano-structures and terahertz lab on-chip system," Acta. Phys. Sin. **65**(1), 010704 (2016).

40. M. Swithenbank, A. D. Burnett, C. Russell, L. H. Li, A. G. Davies, E. H. Linfield, J. E. Cunningham, and C. D. Wood, "On-chip terahertz-frequency measurements of liquids," Anal. Chem. **89**(15), 7981–7987 (2017).

41. R. Smith, A. Jooshesh, J. Y. Zhang, and T. Darcie, "Photoconductive generation and detection of THz-bandwidth pulses using near-field coupling to a free-space metallic slit waveguide," Opt. Express **25**(22), 26492–26499 (2017).

42. P. Gallagher, C. S. Yang, T. Lyu, F. L. Tian, R. Kou, H. Zhang, K. Watanabe, T. Taniguchi, and F. Wang, "Quantum-critical conductivity of the Dirac fluid in graphene," Science **364**(6436), 158–162 (2019).

43. J. W. McIver, B. Schulte, F. U. Stein, T. Matsuyama, G. Jotzu, G. Meier, and A. Cavalleri, "Light-induced anomalous Hall effect in graphene," Nat. Phys. **16**(1), 38–41 (2020).

44. J. O. Island, P. Kissin, J. Schalch, X. M. Cui, S. R. Ul Haque, A. Potts, T. Taniguchi, K. Watanabe, R. D. Averitt, and A. F. Young, "On-chip terahertz modulation and emission with integrated graphene junctions," Appl. Phys. Lett. **116**(16), 161104 (2020).

45. K. Yoshioka, N. Kumada, K. Muraki, and M. Hashisaka, "On-chip coherent frequency-domain THz spectroscopy for electrical transport," Appl. Phys. Lett. **117**(16), 161103 (2020).

46. R. W. McGowan, G. Gallot, and D. Grischkowsky, "Propagation of ultrawideband short pulses of terahertz radiation through submillimeter-diameter circular waveguides," Opt. Lett. **24**(20), 1431–1433 (1999).

47. R. Mendis and D. Grischkowsky, "Plastic ribbon THz waveguides," J. Appl. Phys. **88**(7), 4449–4451 (2000).

48. J. Zhang and D. Grischkowsky, "Waveguide terahertz time-domain spectroscopy of nanometer water layers," Opt. Lett. **29**(14), 1617–1619 (2004).

49. H. Zhan, R. Mendis, and D. M. Mittleman, "Superfocusing terahertz waves below λ/250 using plasmonic parallel-plate waveguides," Opt. Express **18**(9), 9643–9650 (2010).

50. N. Laman, S. S. Harsha, D. Grischkowsky, and J. S. Melinger, "High-resolution waveguide THz spectroscopy of biological molecules," Biophys. J. **94**(3), 1010–1020 (2008).

51. M. A. Unutmaz and M. Unlu, "Spoof surface plasmon polariton delay lines for terahertz phase shifters," J. Lightwave Technol. **39**(10), 3187–3192 (2021).

52. H. Zhang, C. Liang, J. Song, C. Fu, X. Zang, L. Chen, and J. Xie, "Terahertz out-of-plane coupler based on compact spot-size converter," Chin. Opt. Lett. **20**(2), 021301 (2022).

53. J. Jin, Z. Cheng, J. Chen, T. Zhou, C. Wu, and C. Xu, "Reconfigurable terahertz Vivaldi antenna based on a hybrid graphene-metal structure," Int. J. RF Microw. C. E. **30**(5), e22175 (2020).

54. P. D. Cunningham, N. N. Valdesl, F. A. Vallejol, L. M. Hayden, B. Polishak, X.-H. Zhou, J. Luo, A. K.-Y. Jen, J. C. Williams, and R. J. Twieg, "Broadband terahertz characterization of the refractive index and absorption of some important polymeric and organic electro-optic materials," J. Appl. Phys. (Melville, NY, U. S.) **109**(4), 043505 (2011).

55. Z. Yan, L. G. Zhu, K. Meng, W. Huang, and Q. Shi, "THz medical imaging: from in vitro to in vivo," Trends Biotechnol. **40**(7), 816–830 (2022).

56. D. G. Allis, A. M. Fedor, T. M. Korter, J. E. Bjarnason, and E. R. Brown, "Assignment of the lowest-lying THz absorption signatures in biotin and lactose monohydrate by solid-state density functional theory," Chem. Phys. Lett. **440**(4-6), 203–209 (2007).

57. K. Moon, Y. Do, H. Park, J. Kim, H. Kang, G. Lee, and H. Han, "Computed terahertz near-field mapping of molecular resonances of lactose stereo-isomer impurities with sub-attomole sensitivity," Sci. Rep. **9**(1), 16915–8 (2019).

58. G. Zhao, M. Ter Mors, T. Wenckebach, and P. C. M. Planken, "Terahertz dielectric properties of polystyrene foam," J. Opt. Soc. Am. B **19**(6), 1476–1479 (2002).